

The combined effects of buoyancy, rotation, and shear on phase boundary evolution

S. Ravichandran,¹ S. Toppaladoddi,² and J. S. Wettlaufer^{1,3}

¹*Nordita, KTH Royal Institute of Technology and Stockholm University, Stockholm 10691, Sweden*

²*University of Oxford, Oxford OX1 4AL*

³*Yale University, New Haven, Connecticut 06520-8109, USA*

We use well-resolved numerical simulations to study the combined effects of buoyancy, pressure-driven shear and rotation on the melt rate and morphology of a layer of pure solid overlying its liquid phase in three dimensions at a Rayleigh number $Ra = 1.25 \times 10^5$. During thermal convection we find that the rate of melting of the solid phase varies non-monotonically with the strength of the imposed shear flow. In the absence of rotation, depending on whether buoyancy or shear is dominant, we observe either domes or ridges aligned in the direction of the shear flow respectively. Furthermore, we show that the geometry of the phase boundary has important effects on the magnitude and evolution of the heat flux in the liquid layer. In the presence of rotation, the strength of which is characterized by the Rossby number (Ro), we observe that for $Ro = O(1)$ the mean flow in the interior is perpendicular to the direction of the constant applied pressure gradient. As the magnitude of the applied horizontal pressure gradient increases, the geometry of solid-liquid interface evolves from the voids characteristic of melting by rotating convection, to grooves oriented perpendicular to or aligned at an oblique angle to the applied pressure gradient.

I. INTRODUCTION

Fluid motions that accompany solid-liquid phase transitions are ubiquitous in both the natural and engineering environments [1–6]. Such fluid motions are either a result of the generation of unstable density gradients during solidification [7–11], or are externally imposed and thereby influence morphological and/or hydrodynamic instabilities in the system [12–21]. The interactions between fluid flows and phase-changing surfaces underlie our understanding of, among other phenomena, the evolution of Earth’s cryosphere [6, 22], defects in materials castings [23], and production of single crystals for silicon chips [4]. In this study, we focus on understanding the combined effects of buoyancy, rotation, and mean shear on the evolution of a phase boundary of a pure material.

The directional solidification of a pure melt is qualitatively different from that of a multi-component melt. However, there are qualitative similarities in the response of the two systems to externally imposed shear flows [24]. During the solidification of a multi-component melt, solute particles (atoms, molecules or colloids) are rejected into the bulk liquid, which can result in the constitutional supercooling of the liquid adjacent to the phase boundary [25]. This promotes “morphological instability”, which leads to dendritic growth: the formation of a convoluted crystal matrix with a concentrated solution of solute particles trapped in the interstices [4]. This region is called a mushy layer. Depending on the equation of state of the liquid phase and the growth direction relative to the gravitational field, convection within (the “mushy layer mode”) or adjacent to (the “boundary layer mode”) may result [26]. Externally imposed flows can change the nature of these two modes.

Some of the earliest systematic investigations into the effects of a mean shear flow on the directional solidification of binary alloys are due to Delves [12, 13] and Coriell *et al.* [15]. Delves [12, 13] considered the effects

of a parabolic flow on the morphological instability using linear stability analysis. He found that the parabolic flow suppresses the instability, the degree of which depended on material properties. Similarly, Coriell *et al.* [15] studied the effects of a Couette flow on the morphological and thermo-solutal instabilities, and found that the latter is suppressed more than the former (due to the fact that the mode of morphological instability is $O(10^2)$ smaller than the thermo-solutal instability). Furthermore, the use of a Couette flow as the base-state velocity profile in this case may only be locally valid, since the momentum equations are governed by an asymptotic-suction boundary-layer profile [24, 27].

Forth and Wheeler [16] considered the effects of an asymptotic-suction boundary-layer flow on morphological instability during the directional solidification of a binary alloy. They found that under certain conditions, the shear flow inhibits the morphological instability and also leads to the development of travelling waves at the phase boundary. However, the phase boundary was found to have negligible effects on the stability of the shear flow.

In the directional solidification of mushy layers, the fate of any incipient perturbation introduced at the mush-melt interface naturally depends on the interaction between the mushy and boundary-layer modes of convective motion. In order to understand the evolution of such perturbations, Feltham and Worster [17, see also the corrigendum in [28]] considered the effects of flows of inviscid and viscous melts on the mush-melt interface using linear stability analysis. Neglecting buoyancy, they found that the forced flows over a corrugated interface introduce pressure perturbations at the phase boundary, which in turn drive fluid motions in the mushy layer. These fluid motions, in certain cases, were found to amplify the interfacial perturbations. However, the heat flux from the melt was found to have negligible effects on this amplification, and was found to only generate travelling waves at the interface.

Neufeld and Wettlaufer [18, 19] used a combination of linear stability analysis and experiments for a more detailed study of the effects of a shear flow on the convective motions in the mushy layer and bulk melt. The following are their main findings: (i) below a critical strength of the imposed shear flow, the convective motions are moderately suppressed; (ii) above this critical strength, the stability of these convective motions decreases monotonically with increasing shear-flow strength; and (iii) for a sufficiently strong shear flow, quasi-two dimensional striations of zero solid fraction are formed perpendicular to the shear-flow direction at the mush-melt interface. These striations form due to local dissolution and growth of the mushy layer, which result from the interactions between the shear and convective motions within and outside the mushy layer.

In addition to shear flows, several other studies have explored the effects of rotation on the stability of the mush-melt interface and the convective motions inside and outside the mushy layer. Some of the first such studies are those of Sample and Hellawell [29, 30] who experimentally explored the effects of spin and spin-and-precessional motions during directional solidification of $\text{NH}_4\text{Cl}-\text{H}_2\text{O}$ and $\text{Pb}-\text{Sn}$ systems, respectively. Their key findings are: (i) channels in the mushy layer through which solute is expelled into the bulk melt originate close to the mush-melt interface due to perturbations in the solutal boundary layer; (ii) when the mould rotates about an angle to the vertical ($20^\circ - 30^\circ$) at low speeds (< 5 rpm), the induced interfacial shear flow arrests the growth of the perturbations, thereby inhibiting the formation of channels; and (iii) rotation about the vertical axis has very little effect on the evolution of the perturbations. In a related study, Lu and Chen [31] using linear stability analysis showed that the rotation about a vertical axis has an appreciable stabilizing effect only for very large rotation rates ($\sim 10^5$ rpm).

Motivated by the experiments of [30], Chung & Chen used linear stability analysis to study the detailed effects of inclined spin and precessional motions on the stability of the mushy layer [32], the mush-melt interface and the bulk melt [33]. They found that (i) rotation of the system about an inclined axis induces flow parallel to the mush-melt interface in both the mushy layer and the bulk melt. However, the maximum velocity in the bulk is much larger than the maximum velocity in the mushy layer [32]; (ii) the induced velocity in the melt increases with increasing angle of inclination and decreases with rotation rate, but the induced velocity in the mushy layer is only sensitive to the inclination angle and increases with it [32]; (iii) the stabilization of the mushy layer is largely due to the reduction in buoyancy perpendicular to the mush-melt interface [32]; (iv) when there is only precessional motion, the most unstable mode of instability in the mushy layer is in the direction perpendicular to the mush-melt interface. Introducing spin allows the induced flow to explore all directions equally, thereby equally stabilizing all modes [32]; (v) five competing mechanisms

– the (stabilising) reduction of buoyancy and rotation normal to the interface, the (destabilising) component of gravity parallel to the interface, and the (stabilising or destabilising) flow induced by inclination and precession – determine the stability of the bulk melt and the interface [33].

There have been relatively few studies on the effects of buoyancy, mean shear, and rotation on directional solidification of pure melts. Using linear and weakly nonlinear stability analyses and experiments, Davis *et al.* [7] explored the different patterns on the phase boundary that result due to convection. These patterns and the transition between them were further explored experimentally by Dietsche and Müller [8]. Recent studies have focussed on the effects of high Rayleigh-number convection on the phase boundary [34–36]. A detailed discussion of these studies can be found in Toppaladoddi [37].

Hirata *et al.* [38, 39] and Gilpin *et al.* [14] experimentally studied the effects of laminar and turbulent boundary-layer flows on the evolution of phase boundaries between ice and water. Gilpin *et al.* [14] observed that when the conductive heat flux through the ice is less than approximately twice the water-to-ice flux, an initially introduced perturbation at the interface grew and advected downstream, leading to the formation of “rippled” surfaces. The heat transfer rate increased by about 30-60% over these surfaces when compared with a flat interface. These observations were attributed solely to mean shear by Gilpin *et al.* [14], but a recent reanalysis of their data showed that there were substantial buoyancy effects due to anomalous behaviour of water at 4°C in their experiments [24]. Furthermore, a linear stability analysis of the Rayleigh-Bénard-Couette flow over a phase boundary showed that mean shear has a stabilizing effect and buoyancy has a destabilizing effect on the phase boundary [24]. More recently, the interplay between mean shear, buoyancy, and phase boundaries has been further explored in two [37] and three [40] dimensions using direct numerical simulations.

Ravichandran and Wettlaufer [41] explored the combined effects of rotation and thermal convection on the evolution of a phase boundary. They found that the rotation-dominated convection of a pure liquid, which takes the form of columnar vortices [42], melts voids into its overlying solid phase. They showed that the feedback of the melting on the convective flow can arrest the horizontal motion of flow structures like the peripheral streaming flow in wall-bounded rotating convection, and hypothesized that the columnar vortices may also be pinned to the locations of the voids. Furthermore, their study revealed that the degree of interfacial roughness co-varies with the heat flux.

Here, we use direct numerical simulations to study the melting of the solid phase of a pure substance driven by thermal convection of its melt, subject to a constant applied pressure gradient in the horizontal direction and rotation about the vertical axis. The combined effects of shear, rotation, and buoyancy on the evolution of phase

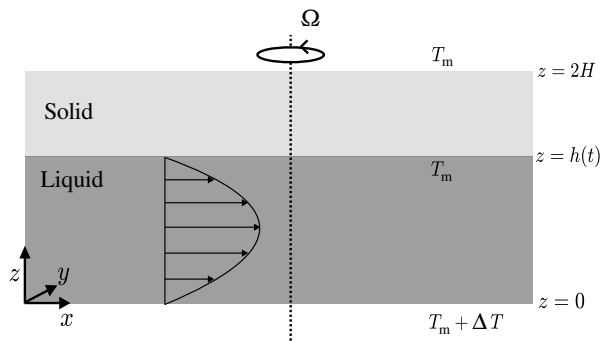


FIG. 1: A vertical cross-section of the geometry considered. The size of the domain is $L \times L \times 2H$, with the aspect ratio $A = L/2H$. The bottom surface is maintained at a higher temperature than the interface.

No-slip and no penetration conditions for the fluid velocity are imposed at the bottom boundary and the evolving interface, and periodic boundary conditions are imposed in the horizontal.

boundaries are important in several geophysical settings [6, 20, 43], and provide important motivations for this study.

The rest of the paper is organised as follows. In §II, we formulate the problem and present the equations of motion along with the initial and boundary conditions. We briefly discuss the numerical method used to solve the equations of motion in §III. We then discuss results from simulations of non-rotating flows in §IV A and of rotation-influenced flows in §IV B. Finally, we conclude with a summary of our observations and suggestions for future work in §V.

II. PROBLEM FORMULATION AND GOVERNING EQUATIONS

In this study, we consider a cuboid of dimensions of $L \times L \times 2H$. The aspect ratio of the cell is defined as $A = L/2H$ and is fixed at either 4 or 8 in the simulations reported here. Figure 1 shows a vertical cross section of the domain. At the initial instant, the planar phase boundary is located at $z = h_0$ and the fluid is contained in the region $0 \leq z \leq h_0$. The bottom plate located at $z = 0$ is maintained at a temperature $T = T_m + \Delta T$. The temperature at the phase boundary is $T = T_m$, and the top plate at $z = 2H$ is maintained at $T = T_m$. We note that because of the isothermal temperature field in the solid phase, it completely melts before a stationary state is reached. Thus, we solely focus on the system dynamics until the solid phase vanishes. Periodic boundary conditions are imposed in the horizontal directions.

The equations of motion in the different regions of the domain are as follows.

A. Liquid

The conservation of momentum, mass and heat are given by

$$\frac{\partial \mathbf{u}}{\partial t} + \mathbf{u} \cdot \nabla \mathbf{u} = -\frac{1}{\rho_0} \nabla p + g \alpha (T - T_m) \hat{\mathbf{z}} - 2\Omega \hat{\mathbf{z}} \times \mathbf{u} + \nu \nabla^2 \mathbf{u} + F_p \hat{\mathbf{x}}, \quad (1)$$

$$\nabla \cdot \mathbf{u} = 0, \text{ and} \quad (2)$$

$$\frac{\partial T}{\partial t} + \mathbf{u} \cdot \nabla T = \kappa \nabla^2 T, \quad (3)$$

respectively. Here, $\mathbf{u}(\mathbf{x}, t) = (u, v, w)$ is the three-dimensional velocity field; ρ_0 is the reference density; $p(\mathbf{x}, t)$ is the pressure field; g is acceleration due to gravity; α is the thermal expansion coefficient; $T(\mathbf{x}, t)$ is the temperature field; the constant pressure gradient is applied as a horizontal body force per unit mass, F_p ; $\hat{\mathbf{x}}$ and $\hat{\mathbf{z}}$ are the unit vectors along the x and z axes, respectively; Ω is the constant speed of rotation; ν is the kinematic viscosity; and κ is the thermal diffusivity.

B. Solid

The entire solid phase is isothermal because of the temperature boundary condition at the upper boundary. Hence, the temperature field in the solid phase is given by

$$T(\mathbf{x}, t) = T_m. \quad (4)$$

C. Evolution of the phase boundary

The location of the phase boundary is determined using the Stefan condition, which is a statement of energy balance [4]:

$$\rho_0 L_s v_n = -\mathbf{n} \cdot \mathbf{q}_l \text{ at } z = h(x, y, t). \quad (5)$$

Here, L_s is the latent heat of fusion; v_n is the normal component of growth rate of the solid phase; \mathbf{n} is the unit normal pointing into the liquid; and \mathbf{q}_l is the heat flux towards the phase boundary from the liquid.

D. Boundary conditions

We impose Dirichlet conditions on temperature at the bottom and top boundaries of the domain:

$$T(x, y, z = 0, t) = T_m + \Delta T \quad \text{and} \quad T(x, y, z = H, t) = T_m, \quad (6)$$

where $\Delta T > 0$. The temperature at the phase boundary is the equilibrium temperature:

$$T(x, y, z = h, t) = T_m. \quad (7)$$

We impose no-slip and no-penetration conditions on the flow velocity at the lower boundary and the phase boundary, given by

$$u(x, y, z = 0, t) = v(x, y, z = 0, t) = w(x, y, z = 0, t) = 0; \quad (8)$$

$$\mathbf{u} \cdot \mathbf{n} = \mathbf{u} \cdot \mathbf{t}_1 = \mathbf{u} \cdot \mathbf{t}_2 = 0 \quad \text{at} \quad z = h(x, y, t), \quad (9)$$

respectively, where \mathbf{t}_1 and \mathbf{t}_2 are the x and y projections of the unit tangents at the phase boundary. We also impose periodic boundary conditions for the temperature and velocity fields at $x = 0$ and $x = L$ and $y = 0$ and $y = L$.

E. Initial conditions

At $t = 0$, the temperature of the liquid layer is maintained at $T(\mathbf{x}, t = 0) = T_m$, and the velocity field is $\mathbf{u}(\mathbf{x}, t = 0) = \mathbf{0}$. The shear flow in the horizontal direction is driven by the body force starting at $t = 0$.

F. Non-dimensional equations of motion

To non-dimensionalize the equations of motion and the associated boundary conditions, we choose H as the length scale; $U_0 = \sqrt{g\alpha\Delta T H}$ as the velocity scale; $t_0 = H/U_0$ as the time scale; $p_0 = \rho_0 U_0^2$ and the pressure scale; and ΔT as the temperature scale. Using these in equations 1 – 3 and 5 and maintaining pre-scaled notation, we get

$$\frac{\partial \mathbf{u}}{\partial t} + \mathbf{u} \cdot \nabla \mathbf{u} = -\nabla p + \sqrt{\frac{Pr}{Ra}} \nabla^2 \mathbf{u} - \frac{2}{Ro} \hat{\mathbf{z}} \times \mathbf{u} + \theta \hat{\mathbf{z}} + \frac{1}{Ri} \hat{\mathbf{x}}, \quad (10)$$

$$\nabla \cdot \mathbf{u} = 0, \quad (11)$$

$$\frac{\partial \theta}{\partial t} + \mathbf{u} \cdot \nabla \theta = \sqrt{\frac{1}{Pr \cdot Ra}} \nabla^2 \theta, \quad \text{and} \quad (12)$$

$$v_n = \sqrt{\frac{1}{Pr \cdot Ra \cdot St^2}} \mathbf{n} \cdot \nabla \theta \quad \text{at} \quad z = h(x, y, t), \quad (13)$$

where the dimensionless temperature,

$$\theta = \frac{T - T_m}{\Delta T}, \quad (14)$$

is defined such that $\theta = 0$ at the phase boundary, and $\theta = 1$ at the heated lower boundary. The five dimensionless

parameters that govern the dynamics of the system are the Rayleigh (Ra), bulk Richardson (Ri_b), Prandtl (Pr), Stefan (St) and Rossby (Ro) numbers, and are defined as

$$Ra = \frac{g\alpha\Delta T H^3}{\nu\kappa}; \quad Ri_b = \frac{g\alpha\Delta T}{F_p}; \quad Pr = \frac{\nu}{\kappa}; \quad (15)$$

$$St = \frac{L_s}{C_p \Delta T}; \quad \text{and} \quad Ro = \sqrt{\frac{g\alpha\Delta T}{\Omega^2 H}}, \quad (16)$$

where C_p is the specific heat of the solid phase. These represent the ratio of buoyancy to viscous forces (Ra), ratio of buoyancy to the imposed horizontal body force per unit mass (Ri_b), ratio of momentum to heat diffusivities (Pr), ratio of the latent to specific heats (St), and the ratio of rotational to convective time scales (Ro). We should note that St is defined based on the temperature difference in the liquid layer and not the solid layer. A bulk Reynolds number can be defined by combining Ra and Ri_b , and is given by

$$Re = \sqrt{\frac{Ra}{Ri_b \cdot Pr}}. \quad (17)$$

The dimensionless temperature boundary conditions are:

$$\theta(x, y, z = 0, t) = 1 \quad \text{and} \quad \theta(x, y, z = H, t) = 0, \quad (18)$$

at the bottom and top surfaces, respectively, and

$$\theta(x, y, z = h, t) = 0, \quad (19)$$

at the phase boundary. The no-slip and no-penetration boundary conditions for the velocity field remain unaltered after the non-dimensionalization.

An important means of quantifying the response of the system is in terms of the Nusselt number, which is defined as the ratio of total heat flux to the heat flux due only to conduction. Following [41], we define the Nusselt number of melting as

$$Nu = \frac{\sqrt{Ra \cdot Pr}}{St} h_s \frac{dh_s}{dt}, \quad (20)$$

where h_s is the horizontally averaged thickness of the solid layer.

III. NUMERICAL METHOD

Equations 11 – 13, along with the boundary conditions, are solved using the finite-volume solver *Megha-5*, with a volume penalization method for the melting solid. The solver uses second-order central differences in space and a second-order Adams-Bashforth time-stepping scheme, and has been extensively validated for free-shear flows

[44, 45] and Rayleigh-Bénard convection [41, 46, 47]. Details of the volume-penalization algorithm, including validation against the analytical solution for the purely conductive Stefan problem, tests of sensitivity to the penalization parameter, and the convergence of the solution under grid-refinement may be found in Ravichandran and Wettlaufer [41]. We have further verified that the body force prescribed in equation 1 produces the known analytical plane-Poiseuille velocity profile with an exponential relaxation timescale of $(\pi^2\nu)^{-1}$ for the peak velocity.

IV. RESULTS

Here, we present our results on the effects of mean shear, buoyancy and rotation on the evolution of the phase boundary. In order to highlight the effects of rotation, we first consider only the effects of mean shear and buoyancy, and later introduce rotation. Unless specified otherwise, we use a grid resolution of at least 64 points per unit length (so that the typical grid size is $1024^2 \times 128$). Furthermore, the results presented here were ascertained to be grid-independent by doubling the number of grid points in the vertical direction for the smallest Ri_b simulations. The penalization parameter is fixed at $\eta \approx 1.4 \times 10^{-3}$, which is sufficiently small for results to be independent of this parameter [41], and the time-step used is $\Delta t \leq 7 \times 10^{-4}$.

A. Zero rotation ($Ro = \infty$)

When rotational effects are absent, the evolution of the phase boundary is affected by the combined action of the mean shear flow and convection. The relative strength of mean shear and buoyancy is quantified using Ri_b : buoyancy dominates when $Ri_b \gg 1$, and mean shear dominates when $Ri_b \ll 1$. We explore the range $Ri_b \in [1, \infty)$ in this section, with the other dimensionless parameters fixed at $Ra = 1.25 \times 10^5$ and $Pr = St = 1$.

In figures 2(a) – 2(d), we show the effects of increasing strength of mean shear flow on the phase boundary at $t = 85$. When mean shear is absent ($Ri_b = \infty$), convective motions tend to create dome-like features at the boundary, which ‘lock-in’ the convection cells. This is seen in figure 2(a). Such features have been investigated in detail in both two [35, 36] and three [34] dimensions. As the strength of the mean shear is increased (decreasing Ri_b), quasi two-dimensional features begin to emerge at the phase boundary. This is seen in figures 2(b) – 2(d). The shear flow, which is parallel to the x -axis, tends to homogenize the phase boundary along the flow direction. However, it does not affect features of the corrugations that are perpendicular to the flow, i.e. parallel to the y -axis [24]. Such features have also been observed in the recent study of Couston *et al.* [40]. The effect of the mean shear flow here is consistent with that in two dimensions, where the corrugations of a phase boundary decrease in

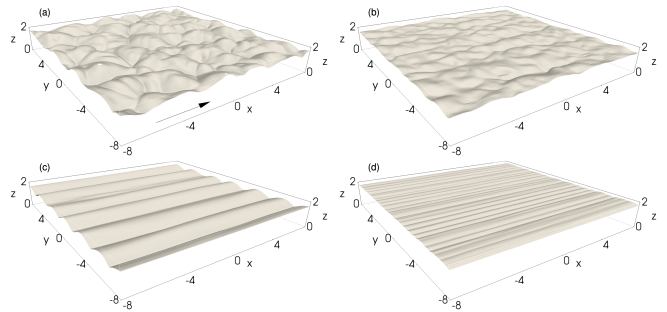


FIG. 2: The solid liquid interface viewed from the solid side for $Ro = \infty$, $Ra = 1.25 \times 10^5$, $Pr = 1$, and $St = 1$ at $t = 85$ for (a) $Ri_b = \infty$, (b) $Ri_b = 100$, (c) $Ri_b = 10$, (d) $Ri_b = 1$. For $Ri_b = \infty$, the melting melts dome-like voids into the solid, as seen in (a). Nascent streamwise alignment of the melting pattern appears for $Ri_b = 100$ in (b). For smaller Ri_b , the formation of quasi-two dimensional grooves separated by sharp furrows is seen in (c) and (d). The arrow in (a) denotes the direction of the shear flow along the x direction.

amplitude as a result of shear [37]. Although these features are qualitatively different from those observed experimentally by [14], their Re based on the boundary-layer thickness was $O(10^4)$, whereas here the bulk Re is $O(10^2 - 10^3)$, making direct regime comparison challenging.

The emergence of streamwise features at the phase boundary as the strength of the mean shear increases can also be seen in the contours of vertical component of the velocity and temperature. These are shown in figures 3 and 4 for $Ri_b = 100$ and 10, respectively. The along-flow homogenization effect of the mean shear flow on the phase boundary is evident from figures 3(c)-(d) and 4(c)-(d), which show grooves aligned with the shear flow. Another interesting feature to note is that with decreasing Ri_b , the corrugations at the phase boundary become more regular in the $y - z$ plane, which is shown in figures 3(f) and 4(f). This indicates that the mean shear flow inhibits vertical motions, which is similar to its effects in two dimensions [37]. For sufficiently strong shear, $Ri_b \lesssim 4$ here, the flow is no longer locked in under the arches, and becomes turbulent and three-dimensional (see figure 5). As a result, the wavelength of the interfacial arches decreases, and they are *less* prominent for $Ri_b = 1$ than for $Ri_b = 4$, although they continue to be aligned in the streamwise-direction. This decoupling of the flow structures and phase-boundary is also discussed in §IV B below.

In figure 6 we show the time evolution of h_s , and Nu for different Ri_b . The melting rate of the solid, ascertained from the slopes of the $h_s(t)$ curves, is a non-monotonic function of Ri_b . When Ri_b is reduced from ∞ to 4, the rate of melting decreases. However, with a further decrease in Ri_b from 4 to 1, there is an increase in the melting rate. This is seen in figure 6(a). This non-

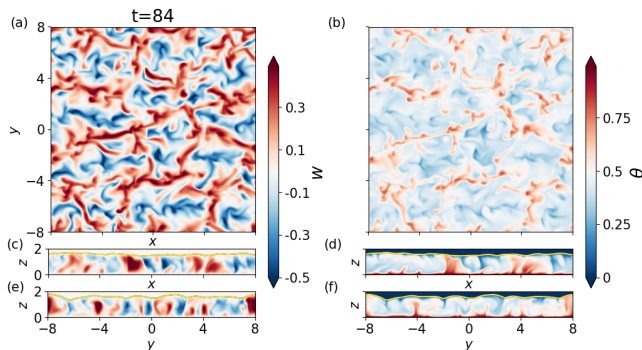


FIG. 3: Contours of vertical velocity w and temperature θ at the horizontal section $z = H/2$ (a,b) and the vertical sections $y = 0$ (c,d) and $x = 0$ (e,f).

The solid-liquid interface is shown in the vertical sections as a solid yellow line. The flow parameters are $Ri_b = 100$, $Ro = \infty$, $Ra = 1.25 \times 10^5$, $Pr = 1$, and $St = 1$.

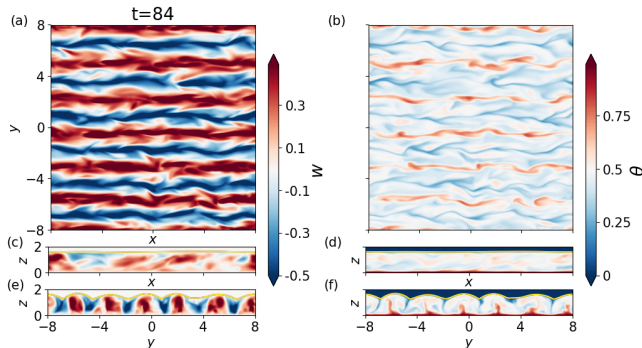


FIG. 4: Contour of vertical velocity w and temperature θ , as in figure 3 and for the same flow parameters except with $Ri_b = 10$. Here, streamwise flow structures are prominent and the melting morphology becomes two-dimensional forming grooves parallel to the x direction (i.e. with a wavenumber perpendicular to the direction of the shear flow).

monotonicity results from the relative dominance of shear flow and convection in the dynamics of the system. For $Ri_b = 100$, the mean shear flow is relatively weak, but acts to inhibit vertical motions. This results in decreased heat transport when compared to the $Ri_b = \infty$ case. This trend continues for $Ri_b = 10$, where the vertical motions are further inhibited. However, a further decrease in Ri_b to 1 results in the mean shear flow becoming dominant, and the Nu and melting rate increase due to the action of forced convection. These effects of decreasing Ri_b can be seen in figures 3(f), 4(f) and 5(f) where the flow field transitions from having distinct plume structures to a more chaotic 3-D flow. The changes reported here are qualitatively consistent with those observed in the study of pure Rayleigh-Bénard-Poiseuille flow in 3-D by [48].

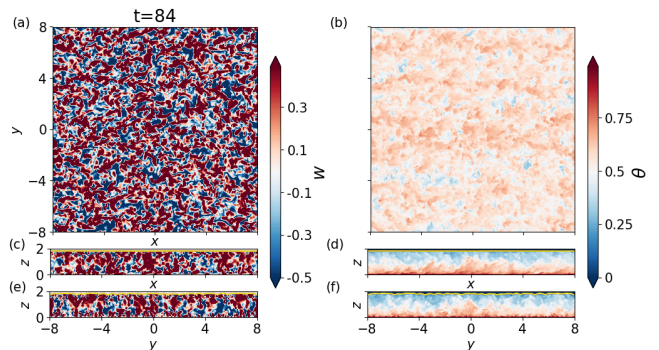


FIG. 5: Contours of vertical velocity w and temperature θ as in figures 3 and 4 and for the same flow parameters except $Ri_b = 1$. The increased shear, compared to $Ri_b = 10$, causes the flow to become fully three-dimensional. This greatly increases the heat transfer rate and the Nusselt number (see also figure 6). As a result, the grooves are *less prominent* (c.f. figure 2).

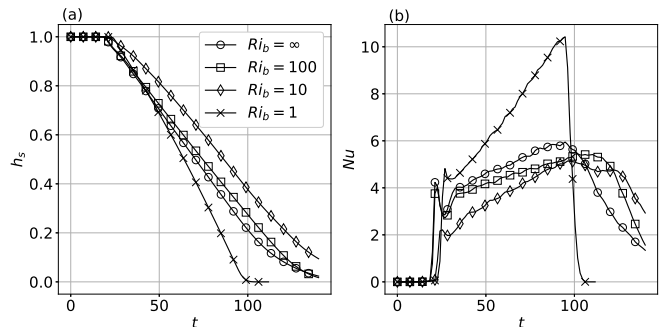


FIG. 6: (a) The thickness of the solid layer h_s as a function of time and (b) the melting Nusselt number (from eq. 20) (b) for $Ro = \infty$, $Ra = 1.25 \times 10^5$, $Pr = 1$, $St = 1$, and varying Ri_b . The rate of melting varies non-monotonically with Ri_b .

B. Finite rotation ($Ro = \mathcal{O}(1)$)

Having studied the effects of mean shear and buoyancy on the flow dynamics, we now consider the effects of rotation. We use the same $Ra = 1.25 \times 10^5$ as in §IV A and fix $Pr = 5$, giving $Ro = 0.6325$, and study the evolution of the flow and the phase boundary for $Ri_b \in [0.1, 100]$. The choice of the higher value of Pr here is to ensure $Ro < 1$ and hence rotational dominance [see, e.g. 41].

In figures 7(a)-(d), we show the phase-boundary geometry for the different values of Ri_b . For $Ri_b = 100$, rotational and buoyancy effects dominate, and the flow and melting morphology are similar to those in the pure rotation-convection case. The flow in this regime consists of columnar vortices spanning the height of the liquid layer that transport heat between the lower and upper boundaries [41, 42]. These vortices melt voids in the solid phase, leading to the formation of dome-like features at

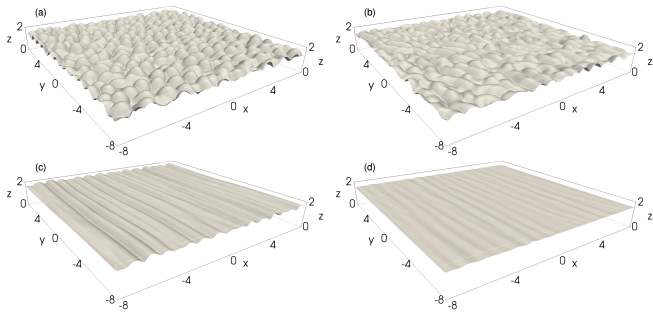


FIG. 7: The solid liquid interface seen from the solid side with flow parameters $Ro = 0.6325$, $Ra = 1.25 \times 10^5$, $Pr = 1$, $St = 1$, and (a) $Ri_b = 100$ at $t = 155$, (b) $Ri_b = 10$ at $t = 155$, (c) $Ri_b = 1$ at $t = 240$, (d) $Ri_b = 0.5$ at $t = 240$. Characteristic melting by rotating convection [see e.g. 41] is seen in (a) for large Ri_b . Compare the effect of large Ri_b for $Ro = \infty$ in figure 2(b), and note that the figures are plotted at different times owing to the differences in the timescales of melting. (b) For $Ri_b = 10$, the lateral drift of the vortices is reflected in the connectivity between neighbouring solid voids to form longer grooves that do not span the width of the domain. (c) For $Ri_b = 1$, the grooves become quasi two-dimensional and span the width of the domain in the lateral direction. (d) For $Ri_b = 0.5$, the grooves are less prominent than in (c).

the phase boundary [41]. This is seen in figure 7(a). For $Ro < 1$, as we have here, the flow in the bulk is governed by the balance of the Coriolis effect and the applied body force. As a result, the flow in the bulk is not in the positive x direction, but rather along the negative y direction. With decreasing values of Ri_b , the imposed shear flow becomes stronger and the columnar vortices move along with the flow in the negative y direction while retaining their coherence. As a result, the domes begin to merge along the y direction, leading to the formation of grooves at the phase boundary. This is seen in figures 7(b) and 7(c), which show the phase boundary geometry for $Ri_b = 10$ and $Ri_b = 1$, respectively. A further decrease in Ri_b to 0.5 causes the grooves in phase boundary to become less prominent, but still aligned along the y -direction, as seen in figure 7(d).

These effects are also reflected in h_s and Nu , whose time evolution is plotted in figures 10(a) and 10(b), respectively, showing that the melt rate and the heat transport decrease with decreasing Ri_b . This is due to the increasing strength of the shear flow that tends to inhibit vertical motions. The decrease in the rate of melting of the solid phase can be discerned from the slopes of the $h_s(t)$ curves in 10(a). We note that the peaks in the $Nu(t)$ curves for $Ri_b = 100$ and 10 occur when the domes have reached the upper boundary [see 41, and their discussion of the correlation between Nu and the interfacial roughness].

For $Ri_b \lesssim 0.2$, the strength of the shear flow causes the

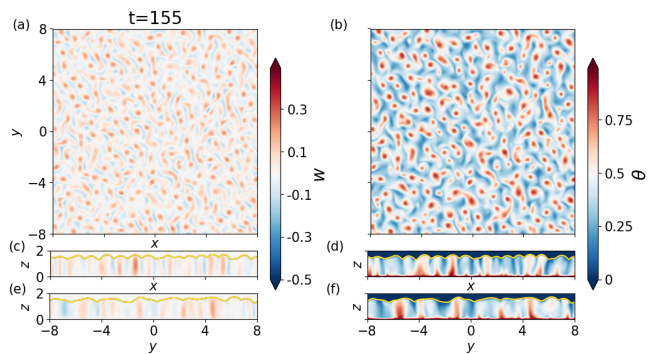


FIG. 8: Contours of vertical velocity w and temperature θ at the horizontal section $z = H/2$ (a,b) and the vertical sections $y = 0$ (c,d) and $x = 0$ (e,f).

The solid-liquid interface is shown in the vertical sections as a solid yellow line. The flow parameters are $Ri_b = 10$, $Ro = 0.6325$, $Ra = 1.25 \times 10^5$, $Pr = 5$, and $St = 1$. Coherent columnar vortices begin to drift in the negative y direction. The corresponding melting morphology is shown in figure 7(a).

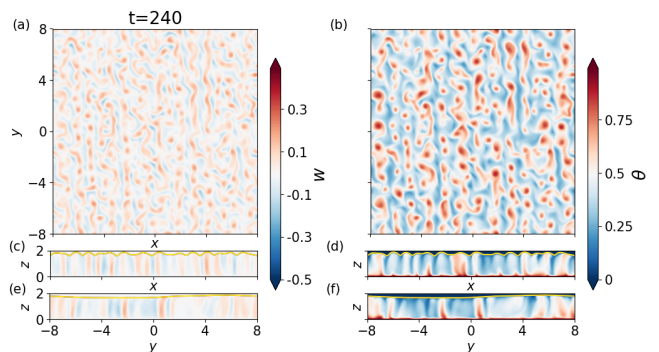


FIG. 9: Contours of vertical velocity w and temperature θ as in figure 8 and for the same parameters except $Ri_b = 1$. The drift velocity of the columnar vortices along the negative y direction is sufficiently strong for the melting morphology to become quasi-two dimensional (compare the vertical sections (e) and (f) to the melting morphology shown in figure 7(c)).

columnar vortices to lose their coherence, and hence the resulting morphology of the phase boundary is markedly different. This is seen in figure 11, which shows the formation of grooves at the phase-boundary for $Ri_b = 0.2$ (figures 11(a) and (b)) and $Ri_b = 0.1$ (figures 11(c) and (d)). However, in stark contrast to the large Ri_b cases, these grooves are aligned neither parallel nor perpendicular to the direction \hat{x} of the applied pressure gradient but at an intermediate angle. We note that even for these large shear amplitudes, the flow in the bulk is along the negative y direction, which is shown in figure 12. The oblique alignment of the grooves is a result of the turning of the flow in the Ekman layers adjacent to the solid

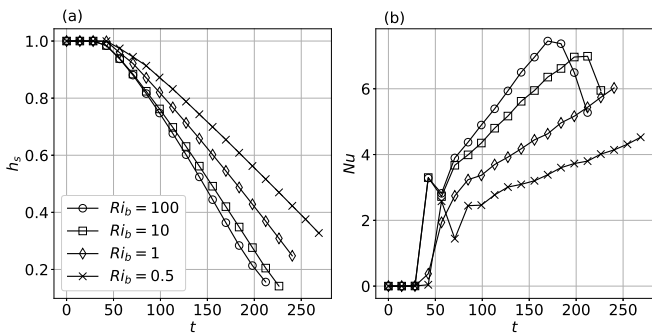


FIG. 10: (a) The thickness of the solid layer h_s and (b) the Nusselt number as a function of time for the cases presented in Figs. 8-9. The rate of melting decreases with decreasing Ri_b .

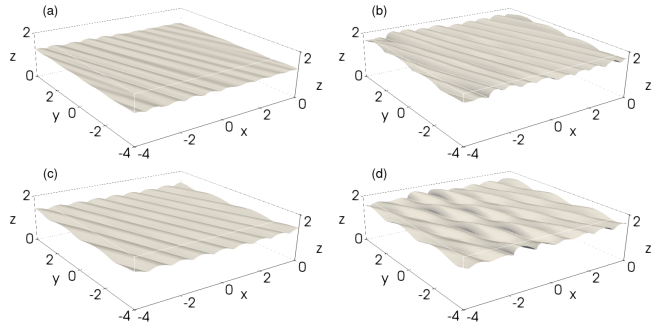


FIG. 11: The morphology of the solid-liquid interface (seen from the solid side) at (a) $t = 354$ and (b) $t = 495$ with $Ri_b = 0.2$ and (c) $t = 495$ and (d) $t = 566$ with $Ri_b = 0.1$. The other parameters are $Ro = 0.6325$, $Ra = 1.25 \times 10^5$, $Pr = 5$, and $St = 1$. As melting proceeds, the grooves are aligned in a direction intermediate between the x and y directions, with a smaller angle between the grooves and the x axis for smaller Ri_b . At late times, the interface develops a sinusoidal mode parallel to the grooves. The initial liquid height $h_0 = 0.5$ in these simulations.

boundary. Contour plots of the vertical velocity and temperature (figure 13) show that the flow in the bulk is quasi-two dimensional. At late times, the grooves develop a sinusoidal mode along the groove direction, as seen in figures 11(b) and (d), but more prominently in the latter. Figure 14 shows that the appearance of this sinusoidal mode is accompanied by a significantly larger melt rate and a corresponding increase in the Nusselt number.

The different phase-boundary geometries suggest the existence of four distinct regimes: (1) In the first regime ($Ri_b \gg 1$), the mean shear flow is weak and rotation and buoyancy dominate, leading to columnar vortices and dome-like features at the phase boundary; (2) In the second ($Ri_b = O(1)$), the mean shear flow is stronger and the columnar vortices are advected with the flow (see figures 8(a) and 8(b)). This is reflected in the phase bound-

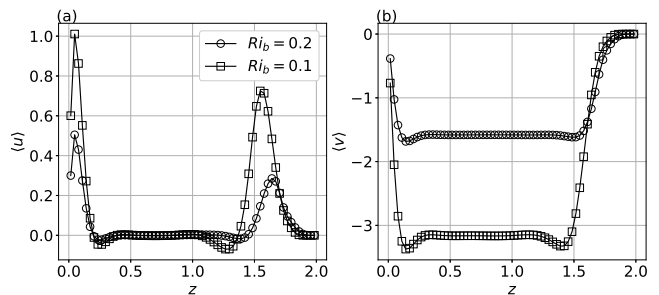


FIG. 12: The horizontally averaged mean values of the velocities u (a) and v (b) along the x and y directions respectively, for $Ri_b = 0.2$ at $t = 495$ and $Ri_b = 0.1$ at $t = 566$ corresponding to the snapshots in figures 11 (b) and (d), as indicated by the labels for Ri_b in the inset. In the bulk, the velocity is nearly perpendicular to the applied pressure gradient.

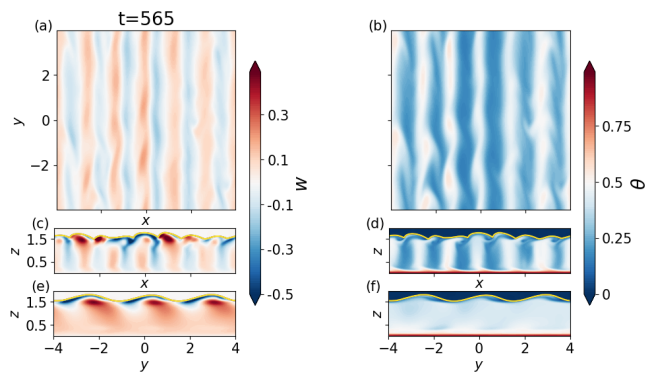


FIG. 13: Contours of vertical velocity w and temperature θ as in figures 8 and 9, and for the same parameters except $Ri_b = 0.1$ and initial liquid layer height $h_0 = 0.5$. The columnar vortices are no longer distinguishable and have merged to produce two-dimensional rolls in the bulk (see also figure 12). The turning of the flow in the Ekman layers creates the grooves aligned at an angle intermediate between the x and y directions.

ary geometry which shows incipient grooves perpendicular to the direction of the shear flow (figures 7(b,c) and 8(a,b) and 9(a,b)); (3) In the third regime ($Ri_b \lesssim 0.5$), strong shear leads to the loss of coherence of the columnar vortices, resulting in their partial merger, while the interfacial grooves become less prominent. This is seen in figure 7(d); (4) And, in the fourth regime, with $Ri_b \lesssim 0.2$, the columnar vortices merge completely and convective motions become quasi-two dimensional in the bulk. The flow in these cells is turned counter-clockwise in the Ekman layers, leading to the formation of grooves aligned at an angle to the direction of the bulk shear flow and becoming sinusoidal.

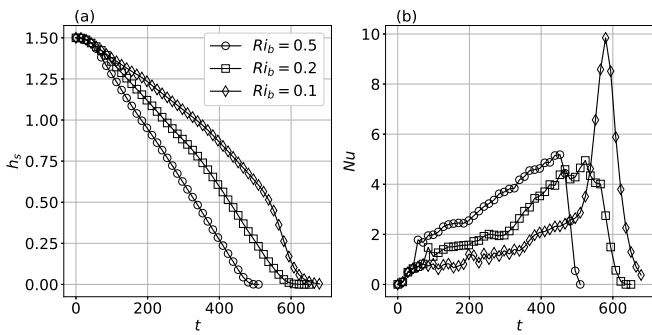


FIG. 14: (a) The thickness of the solid layer and (b) the Nusselt number as a function of time for $Ro = 0.6325$, $Ra = 1.25 \times 10^5$, $Pr = 5$, $St = 1$, and three different values of Ri_b . The overall rate of melting is initially smaller for smaller Ri_b , but as the flow develops, the Nusselt number increases sharply with the development of the along-groove sinusoidal mode. Also note the abrupt change in the slope of the thickness curve for $Ri_b = 0.1$ at $t \approx 565$, which coincides with the increase in Nu .

V. CONCLUSIONS

We have systematically explored the effects of buoyancy, rotation, and shear on the evolution of a phase boundary using direct numerical simulations in three dimensions with flow parameters (a) $Ro = \infty, 1$; (b) $Ra = 1.25 \times 10^5$; (c) $St = 1$; (e) $Pr = 1, 5$; and (f) $Ri_b \in [0.1, \infty)$. The main conclusions from our study are as follows.

(1) In the absence of rotation ($Ro = \infty$), we observe either dome-like features or grooves on the phase boundary depending on whether buoyancy or mean shear dominates the flow. In particular, we find the following three features.

1. As the value of Ri_b decreases from ∞ , the strength of the shear flow increases and both the flow structure and phase boundary geometry transition from three- to quasi-two-dimensional. This is seen in figures 2, 3(a)-(b), and 4(a)-(b).
2. For small Ri_b the grooves formed on the phase boundary are aligned parallel to the direction of the shear flow. This is in agreement with the numerical results of Couston *et al.* [40], but in contrast to the experimental results of Gilpin *et al.* [14]. In our simulations, the bulk $Re = O(10^2 - 10^3)$, whereas in the experiments of Gilpin *et al.* [14] the Re based on the boundary-layer thickness is $O(10^4)$, so that the flow regimes are not directly comparable.
3. The heat transport is a non-monotonic function of Ri_b . For $Ri_b \in [10 - 100]$, the mean shear flow is weaker than buoyancy, but nonetheless inhibits vertical motions, leading to smaller melt rates and vertical heat transport. On further decreasing Ri_b

to 1, the flow becomes three-dimensional and enters the forced turbulent convection regime. This results in larger heat transport and hence an increased melt rate.

(2) When rotation is introduced ($Ro = 0.6325$), the mean flow in the interior is in geostrophic balance and thus in a direction perpendicular to the direction of the applied pressure gradient.

1. For $Ri_b \gg 1$, the shear flow is weak and the phase-boundary consists of dome-like features.
2. As Ri_b is decreased to $O(1)$ values, the columnar vortices are advected by the shear but maintain their coherence.
3. Reducing Ri_b further ($0.2 \lesssim Ri_b \lesssim 0.5$) increases the velocity at which the columnar vortices drift, and the domes on the phase boundary merge and lead to the formation of grooves aligned perpendicular to the applied pressure gradient.
4. And for $Ri_b \lesssim 0.2$, the columnar vortices lose their coherence leading to a quasi-two-dimensional flow in the bulk, and the grooves become sinusoidal and align at an oblique angle to the applied pressure gradient. This feature leads to enhanced heat transport between the fluid and the solid.

Our results suggest several avenues for further research. With or without rotation, our findings suggest that a secondary instability disrupts the basic flow state in which the applied pressure gradient is balanced by other forces in the flow. The mechanism of the instability, and the boundary between the quasi-two dimensional state and the three dimensional state are compelling foci for further study. In particular, in rotating convection, the competition between the geostrophic bulk and the viscous Ekman layers is crucial in determining the state of the flow and the concomitant heat transport, and has thus been a question of significant interest in the literature [49, 50]. Here, however, this competition is reflected in the morphology of the solid-liquid interface, with either the bulk flow or the Ekman boundary layers controlling the alignment of the observed grooves. Therefore, the manner in which the free boundary reflects the state of the flow and the associated flow-geometry feedback, provide an ideal testing ground for general questions in rotating convection and a framework for the wide range of settings in which such flows accompany phase changes.

ACKNOWLEDGEMENTS

Computational resources from the Swedish National Infrastructure for Computing (SNIC) under grants SNIC/2019-3-386 and SNIC/2020-5-471 are gratefully acknowledged. Computations were performed on Tetralith. S.R. and J.S.W. acknowledge support from

Swedish Research Council under grant no. 638-2013-9243, and S.T. acknowledges a Research Fellowship from All Souls College, Oxford.

DECLARATION OF INTERESTS

The authors report no conflict of interest.

-
- [1] M. Epstein and F. B. Cheung, *Ann. Rev. Fl. Mech.* **15**, 293 (1983).
- [2] M. E. Glicksman, S. R. Coriell, and G. B. McFadden, *Annu. Rev. Fl. Mech.* **18**, 307 (1986).
- [3] H. E. Huppert, *J. Fluid Mech.* **173**, 557 (1986).
- [4] M. G. Worster, in *Perspectives in Fluid Dynamics — a Collective Introduction to Current Research*, edited by G. Batchelor, H. Moffatt, and M. Worster (Cambridge University Press, 2000) pp. 393 – 446.
- [5] P. Meakin and B. Jamtveit, *Proc. R. Soc. A* **466**, 659 (2009).
- [6] I. J. Hewitt, *Annu. Rev. Fl. Mech.* **52**, 145 (2020).
- [7] S. H. Davis, U. Müller, and C. Dietsche, *J. Fluid Mech.* **144**, 133 (1984).
- [8] C. Dietsche and U. Müller, *J. Fluid Mech.* **161**, 249 (1985).
- [9] J. S. Wettlaufer, M. G. Worster, and H. E. Huppert, *J. Fluid Mech.* **344**, 291 (1997).
- [10] M. G. Worster, *Ann. Rev. Fl. Mech.* **29**, 91 (1997).
- [11] M. S. Davies Wykes, J. M. Huang, G. A. Hajjar, and L. Ristroph, *Phys. Rev. Fluids* **3**, 043801 (2018).
- [12] R. T. Delves, *J. Cryst. Growth* **3**, 562 (1968).
- [13] R. T. Delves, *J. Cryst. Growth* **8**, 13 (1971).
- [14] R. R. Gilpin, T. Hirata, and K. C. Cheng, *J. Fluid Mech.* **99**, 619 (1980).
- [15] S. R. Coriell, G. B. McFadden, R. F. Boisvert, and R. F. Sekerka, *J. Cryst. Growth* **69**, 15 (1984).
- [16] S. A. Forth and A. A. Wheeler, *J. Fluid Mech.* **202**, 339 (1989).
- [17] D. L. Feltham and M. G. Worster, *J. Fluid Mech.* **391**, 337 (1999).
- [18] J. A. Neufeld and J. S. Wettlaufer, *J. Fluid Mech.* **612**, 363 (2008).
- [19] J. A. Neufeld and J. S. Wettlaufer, *J. Fluid Mech.* **612**, 339 (2008).
- [20] E. Ramudu, B. H. Hirsh, P. Olson, and A. Gnanadesikan, *J. Fluid Mech.* **798**, 572 (2016).
- [21] M. Bushuk, D. M. Holland, T. P. Stanton, A. Stern, and C. Gray, *J. Fluid Mech.* **873**, 942 (2019).
- [22] M. G. McPhee, *Air-Ice-Ocean Interaction: Turbulent Ocean Boundary Layer Exchange Processes* (Springer, New York, NY, 2008).
- [23] W. Kurz and D. J. Fischer, *Fundamentals of Solidification* (Trans Tech Publications, Switzerland-Germany-UK- USA, 1984).
- [24] S. Toppaladoddi and J. S. Wettlaufer, *J. Fluid Mech.* **868**, 648 (2019).
- [25] M. G. Worster, S. S. L. Peppin, and J. S. Wettlaufer, *J. Fluid Mech.* **914**, A28 (2021).
- [26] M. G. Worster, *J. Fluid Mech.* **237**, 649 (1992).
- [27] P. G. Drazin and W. H. Reid, *Hydrodynamic Stability* (Cambridge University Press, Cambridge, 2004).
- [28] J. A. Neufeld, J. S. Wettlaufer, D. L. Feltham, and M. G. Worster, *J. Fluid Mech.* **549**, 442 (2006).
- [29] A. Sample and A. K. Hellowell, *Metall. Trans. B* **13**, 495 (1982).
- [30] A. K. Sample and A. Hellowell, *Metall. Trans. A* **15**, 2163 (1984).
- [31] J. W. Lu and F. Chen, *Int. J. Heat Mass Transfer* **40**, 237 (1997).
- [32] C. A. Chung and F. Chen, *J. Fluid Mech.* **412**, 93 (2000).
- [33] C. A. Chung and F. Chen, *J. Fluid Mech.* **477**, 381 (2003).
- [34] B. R. Esfahani, S. C. Hirata, S. Berti, and E. Calzavarini, *Phys. Rev. Fluids* **3**, 053501 (2018).
- [35] B. Favier, J. Purseed, and L. Duchemin, *J. Fluid Mech.* **858**, 437 (2019).
- [36] J. Purseed, B. Favier, L. Duchemin, and E. W. Hester, *Phys. Rev. Fluids* **5**, 023501 (2020).
- [37] S. Toppaladoddi, *J. Fluid Mech.* **919**, A28 (2021).
- [38] T. Hirata, R. R. Gilpin, and K. C. Cheng, *Int. J. Heat Mass Transfer* **22**, 1435 (1979).
- [39] T. Hirata, R. R. Gilpin, K. C. Cheng, and E. M. Gates, *Int. J. Heat Mass Transfer* **22**, 1425 (1979).
- [40] L.-A. Couston, E. Hester, B. Favier, J. R. Taylor, P. R. Holland, and A. Jenkins, *J. Fluid Mech.* **911**, A44 (2020).
- [41] S. Ravichandran and J. Wettlaufer, *J. Fluid Mech.* **916**, A28 (2021).
- [42] H. T. Rossby, *J. Fluid Mech.* **36**, 309 (1969).
- [43] M. G. Wells and J. S. Wettlaufer, *Geophys. Res. Lett.* **35**, L03501 (2008).
- [44] R. Singhal, S. Ravichandran, S. S. Diwan, and G. L. Brown, in *Proceedings of 16th Asian Congress of Fluid Mechanics* (Springer, 2021) pp. 403–411.
- [45] R. Singhal, S. Ravichandran, R. Govindarajan, and S. S. Diwan, arXiv:2103.16415 (2021).
- [46] S. Ravichandran, E. Meiburg, and R. Govindarajan, *J. Fluid Mech.* **899** (2020).
- [47] S. Ravichandran and J. S. Wettlaufer, *J. Fluid Mech.* **897** (2020).
- [48] A. Scagliarini, Á. Gylfason, and F. Toschi, *Phys. Rev. E* **89**, 043012 (2014).
- [49] E. M. King, S. Stellmach, and J. M. Aurnou, *J. Fluid Mech.* **691**, 568 (2012).
- [50] K. Julien, E. Knobloch, A. M. Rubio, and G. M. Vasil, *Phys. Rev. Lett.* **109**, 254503 (2012).